

NATIONAL INSTITUTE FOR FUSION SCIENCE

Macroscale Implicit, Electromagnetic Particle Simulation of Inhomogeneous and Magnetized Plasmas in Multi-Dimensions

M. Tanaka, S. Murakami, H. Takamaru and T. Sato

(Received – May 17, 1991)

NIFS-91

Jun. 1991

RESEARCH REPORT **NIFS Series**

This report was prepared as a preprint of work performed as a collaboration research of the National Institute for Fusion Science (NIFS) of Japan. This document is intended for information only and for future publication in a journal after some rearrangements of its contents.

Inquiries about copyright and reproduction should be addressed to the Research Information Center, National Institute for Fusion Science, Nagoya 464-01, Japan.

NAGOYA, JAPAN

Macroscale Implicit, Electromagnetic Particle Simulation of Inhomogeneous and Magnetized Plasmas in Multi-Dimensions

Motohiko Tanaka, S.Murakami^{*)}, H.Takamaru^{*)} and T.Sato

National Institute for Fusion Science, Nagoya 464-01, Japan
Faculty of Science, Hiroshima University, Hiroshima 730, Japan^{*)}

Abstract

An implicit, electromagnetic particle (kinetic) simulation method is presented that can deal with multi-dimensional, inhomogeneous and finite beta plasmas in large space and time scales. To include the diamagnetic effects in strongly magnetized ($\omega_{ce} \geq \omega_{pe}$) and inhomogeneous, kinetic plasmas of the large scales, full-implicit "directly-coupled field-particle equations" are derived by using the backward time-decentered scheme and the guiding center approximation with the magnetic drifts about the electron perpendicular motion. This algorithm has been implemented for studies of inhomogeneous and magnetized plasmas of three-dimensions. The basic algorithm of the code is described and several physics applications are shown for the Alfvén-ion-cyclotron instability and kink instability of the peaked density ion beam.

Keywords: implicit particle simulation, electromagnetic, MHD scales,
inhomogeneous plasma, nonlinear process

1 Introduction

Many people have noticed an existence of the giant gap in space and time between the microscopic (kinetic) and macroscopic (magnetohydrodynamic) natures of plasmas. Due to the difference in the physical parameters, it was virtually impossible to treat these two regimes simultaneously in a self-consistent manner. Nevertheless, many important and interesting problems of space and fusion plasmas fall on this category. For example, the anomalous transport and its control are of vital importance for the success of magnetically confined fusion but its mechanism has not been well identified. In space physics, there are also varieties of plasma phenomena that belong to this macroscale kinetic regime. Typical of them are the magnetosonic shocks with the ion scale length and the kinetic Alfvén wave that causes substantial wave-particle interactions through its longitudinal electric field.

The aforementioned large space-scale and low frequency plasma phenomena occurring between the microscopic and macroscopic regimes could be adequately studied by neither the traditional (explicit) particle code nor the MHD simulation method. Extensive efforts were made in the 1980's in the United States and Japan to develop new simulation tools to overcome this difficulty. After the decade of research and development, "the moment implicit", "macroscale electromagnetic" and "gyrokinetic" particle simulations seem to be promising among them.

The moment implicit method derives implicit moment equations relying on the concept used in the fluid dynamics and predicts the future electromagnetic field from the lowest two velocity moments. These moments are calculated by summations over the particles. This type of the code known as "the Venus code" was developed in Los Alamos National Laboratory in early 80's and was successfully applied to laser irradiation and various beam-plasma processes¹⁾. This method was recently modified in one-dimension to avoid the iterative solution of the electromagnetic field by taking higher terms in the Taylor expansion into account²⁾.

The macroscale particle simulation³⁾ (MACROS) developed by the author since

early 1984 has been constructed on the physical insight that the backward time-decentered electromagnetic field acts to selectively suppress high frequency oscillations of plasma particles. The macroscale particle code has many favorable common features with the Venus code for large-scale simulations; both of the codes adopt the backward time-decentered scheme. The difference is that the macroscale particle simulation utilizes the particle nature directly that is contained in the original Newton-Maxwell equations. Therefore the macroscale particle simulation is less restrictive about the time step size. These characteristics are realized by virtue of the implicitness of "directly-coupled field-particle equations" which are the equations to determine the future electromagnetic field.

It is noted in passing that the macroscale particle simulation is qualitatively different from the magnetostatic (Darwin) algorithm which uses $\nabla \times \mathbf{B} = (4\pi/c)\mathbf{j}_T$ instead of the full Maxwell equations. The latter requires complete separation of the transverse current \mathbf{j}_T ($\nabla \cdot \mathbf{j}_T = 0$) from the longitudinal one; otherwise numerical instability results. Furthermore, the Darwin algorithm is essentially an explicit model which is bound by $\omega_{pe}\Delta t \leq 1$ and $\Delta x/\lambda_{De} \leq 1$.

The concept of the gyrokinetic simulation⁴⁾ which was initially motivated in the Princeton Plasma Physics Laboratory is different from the previous implicit methods in the point that it is based on the smallness ϵ -ordering on the wavelengths and the amplitude of the electromagnetic field. Many terms are dropped from the original kinetic equations following the ordering. Therefore, this type of the code is correct and efficient when the smallness ordering assumptions are fully satisfied. However, when the assumptions are marginally satisfied, many corrective terms should be taken into account to make the simulation physically meaningful.

When we concentrate our attention to the "kinetic" transport processes occurring in fusion and space plasmas with "macro" (MHD)-scales, we can list up several requirements to be satisfied by the simulation codes. First, the simulation code must have an ability of handling the kinetic plasmas in multi-dimensions where the space and time scales are not microscopic, *i.e.*, $\omega_{pe}\Delta t \gg 1$ and $\Delta x \geq c/\omega_{pe} \gg \lambda_{De}$. Second, magneti-

cally confined plasmas are strongly magnetized ($\omega_{ce} \geq \omega_{pe}$) and quite inhomogeneous in density; the magnetic field changes its orientation and strength in space. Moreover, the diamagnetic effects are not ignorable to treat the finite beta (temperature) plasmas.

An intermediate, so-called semi-implicit version of the macroscale particle simulation code was finished by 1986. This version of the code is applicable to plasmas with the magnetic null points and was actually applied to variety of studies such as excitation of the kinetic Alfvén wave /plasma heating⁵⁾, and current-beam injection /kink instability⁶⁾. Although these studies were virtually the first to have ever been made by the large-scale, kinetic simulation code of general purposes, the time step was limited to $\omega_{pe}\Delta t \leq 1$ due to the predictor-corrector method adopted to calculate the future current density in the field equation. (Full implicitness is violated here.)

The macroscale particle simulation code that can deal with homogeneous plasmas in large space and time scales was completed by 1988. The validity of the algorithm was extensively studied and verified both analytically and numerically³⁾. However, this version did not include the diamagnetic drift current and the field iteration failed for a plasma with large density inhomogeneity. Recently the old version of the macroscale particle simulation code has been upgraded to deal with inhomogeneous kinetic plasmas in large (MHD) scales. Specifically, the drift approximation with the magnetic drifts has been introduced to the "perpendicular" motion of the electrons; the electron cyclotron time scale is as short as that of the Langmuir oscillations, *i.e.*, $\omega_{ce} \sim \omega_{pe}$ for magnetically confined plasmas. By contrast, the parallel part of the electron motion is traced exactly as the particle species. The slightly backward time-decentered scheme is used as before, both in the equations of motion and the Maxwell equations to attenuate high frequency oscillations in the plasma.

The characteristic features of the macroscale particle simulation code thus developed are summarized in Table 1. One of the important features here is that low frequency, electromagnetic (electrostatic, of course) waves and structures with $\omega\Delta t < 1$ are properly reproduced where ω is their characteristic frequency. Therefore, Landau and cyclotron resonance effects are included in the code. Since full particle dynamics

are retained for the ions and the parallel part of the electron motion (on top of the drift motion in the perpendicular direction), various particle orbit effects in the inhomogeneous plasmas, such as finite Larmor radius effect, banana and trapped orbit effects in the torus geometry, are included in the macroscale particle code. Moreover, the code is numerically stable both in linear and nonlinear stages by virtue of the simple backward time-decentered scheme adopted. These characteristic features make the macroscale particle simulation method quite suitable for studies of large space and time-scale, kinetic and nonlinear processes occurring in magnetized plasmas.

As will be described in Sec.2, the key of the code is that it is completely implicit in time. In order to get rid of the Courant condition that severely limits the time step for given space grid intervals, the Maxwell equations are directly coupled with the equations of motion of particles. This procedure results in the full-implicit "directly-coupled field-particle (DCFP) equations." The macroscale particle simulation may be thus called "directly-coupled implicit method" in a technical sense. A special iterative technique is devised to solve this coupled field-particle equations for inhomogeneous density plasmas; the iteration converges in a few cycles in one-dimension, and in a couple of ten cycles in three-dimensions.

In the next section, the algorithm of the macroscale particle code will be described for the simulation of inhomogeneous, magnetized plasmas in multi-dimensions. Several physics applications to large-scale, kinetic problems will be shown in Sec.3 and 4.

2 General Algorithm

2.1 Field and particle equations

The foregoing characteristic features of the macroscale particle simulation are realized partly by the introduction of the slightly backward time-decentered scheme both into the Maxwell equations and the equations of motion of particles³⁾. The Maxwell

equations with the time level suffices are given by

$$\frac{1}{c} \left(\frac{\partial \mathbf{E}}{\partial t} \right)^{n+1/2} = \nabla \times \mathbf{B}^{n+\alpha} - \frac{4\pi}{c} \mathbf{j}^{n+\gamma}, \quad (1)$$

$$\frac{1}{c} \left(\frac{\partial \mathbf{B}}{\partial t} \right)^{n+1/2} = -\nabla \times \mathbf{E}^{n+\alpha}, \quad (2)$$

$$\nabla \cdot \mathbf{E}^{n+1} = 4\pi \rho^{n+1}, \quad (3)$$

$$\nabla \cdot \mathbf{B}^{n+1} = 0. \quad (4)$$

The equations of motion for the ions are,

$$\frac{d\mathbf{v}_j^{n+1/2}}{dt} = \frac{e_i}{m_i} [\mathbf{E}^{n+\alpha}(\mathbf{x}_j) + \frac{\mathbf{v}_j^{n+1/2}}{c} \times \mathbf{B}^{n+\alpha}(\mathbf{x}_j)], \quad (5)$$

$$\frac{d\mathbf{x}_j^{n+1/2}}{dt} = \mathbf{v}_j^{n+1/2}, \quad (6)$$

and the equations of motion for the electrons are,

$$\frac{dv_{\parallel j}^{n+1/2}}{dt} = \frac{(-e)}{m_e} E_{\parallel}^{n+\alpha}(\mathbf{x}_j) - \frac{\mu_j}{m_e} \nabla_{\parallel} B^{n+\alpha}, \quad (7)$$

$$\mathbf{v}_{\perp j}^{n+\gamma} = c \left(\frac{\mathbf{E} \times \mathbf{B}}{B^2} \right)^{n+\gamma} + \left[\left(\frac{m_e c}{-e B} \right) \mathbf{b} \times \left\{ \frac{\mu_j}{m_e} \nabla B + v_{\parallel}^2 (\mathbf{b} \cdot \nabla) \mathbf{b} \right\} \right]^{n+\gamma}, \quad (8)$$

$$\frac{d\mathbf{x}_j^{n+1/2}}{dt} = (\mathbf{v}_{\parallel j}^{n+1/2} + \mathbf{v}_{\perp j}^{n+\gamma}), \quad (9)$$

where $\mathbf{b} = (\mathbf{B}/B)$ is the unit vector along the magnetic field line, and the direction of the parallel velocity of the electrons is defined by

$$\mathbf{v}_{\parallel j}^{n+1/2} = v_{\parallel j}^{n+1/2} \mathbf{b}^{n+1/2}(\mathbf{x}_j). \quad (10)$$

The $E \times B$, gradient-B and the curvature drift terms are incorporated in the perpendicular motion of the electrons.

The parameters α and γ which appear in Maxwell equations and the equations of motion are the implicitness parameters that are chosen slightly larger than $\frac{1}{2}$ depending on trade-off between the accuracy and stability of the code. The decentering shift of the

time level of the curl terms in Eqs.(1)(2) causes damping of high frequency light waves and that of the current density in Eq.(1) results in attenuation of high frequency plasma waves. Damping of high frequency electrostatic waves with $\omega \sim \omega_{pe}$ is attributed to the decentering shift of the field's time level in the equations of motion. It was proved both analytically and numerically that the decentering shift of the $E \times B$ term in Eq.(9) is a necessary condition for the numerical stability³⁾.

It should be noted that the guiding-center approximation is made just for the "perpendicular" part of the electron motion in order to eliminate the electron cyclotron time scale ω_{ce} . By contrast, the ion and electron parallel motions are traced exactly as the particle species. These treatments make this code appropriate for the study of kinetic plasma transport in magnetically confined fusion plasmas for which the relation $\omega_{ce} \sim \omega_{pe} \gg \omega_{ci}$ holds. It may be a natural extension of the present code to introduce the guiding center approximation also to the ions which enables us simulations with a yet larger time scale with $\omega_{ci}\Delta t \gg 1$ at an expense of some physics on ions.

2.2 Equations in the finite difference form

The techniques that make the present implicit algorithm realistic are shown here. The equation of motion for the ions in the finite difference form is written as

$$\mathbf{v}_j^{n+1} = \mathbf{v}_j^n + \Delta t \frac{e_i}{m_i} [\mathbf{E}^{n+\alpha}(\tilde{\mathbf{x}}_j^{n+\gamma}) + \frac{\mathbf{v}_j^{n+1/2}}{c} \times \mathbf{B}^{n+\alpha}(\tilde{\mathbf{x}}_j^{n+\gamma})]. \quad (11)$$

If Eq.(11) is solved in terms of \mathbf{v}_j^{n+1} using the interpolation $\mathbf{v}^{n+1/2} = \frac{1}{2}(\mathbf{v}^n + \mathbf{v}^{n+1})$, then we have

$$\mathbf{v}_j^{n+1} = \mathbf{v}_j^n + \Delta t \frac{e_i}{m_i} [\mathbf{E}^{n+\alpha} + \{ \frac{\mathbf{v}_j^n}{c} + \frac{\Delta t}{2} \frac{e_i}{m_i c} \left(\mathbf{E}^{n+\alpha} + \frac{\mathbf{v}_j^n}{c} \times \mathbf{B}^{n+\alpha} \right. \quad (12)$$

$$\left. + \frac{\Delta t}{2} \frac{e_i}{m_i c} \mathbf{E}^{n+\alpha} \times \mathbf{B}^{n+\alpha} \right) \} \times \frac{\mathbf{B}^{n+\alpha}}{1 + \left(\frac{\Delta t}{2} \frac{e_i B}{m_i c} \right)^2}], \quad (13)$$

$$\mathbf{x}_j^{n+1} = \mathbf{x}_j^n + \Delta t \mathbf{v}_j^{n+1/2}. \quad (14)$$

Similarly, the equations of motion for the electrons are written as

$$v_{\parallel b}^{n+1} = v_{\parallel b}^n + \Delta t \left[\frac{(-e)}{m_e} E_{\parallel}^{n+\alpha}(\tilde{\mathbf{x}}_j^{n+\gamma}) - \frac{\mu_j}{m_e} \nabla_{\parallel} B^{n+\alpha} \right], \quad (15)$$

$$\mathbf{x}_j^{n+1} = \mathbf{x}_j^n + \Delta t [\mathbf{v}_{\parallel b}^{n+1/2} + \mathbf{v}_{\perp j}^{n+\gamma}(\tilde{\mathbf{x}}_j^{n+\gamma})]. \quad (16)$$

The field is evaluated at the "predicted" position $\tilde{\mathbf{x}}_j^{n+\gamma} = \mathbf{x}_j^n + \gamma \Delta t \mathbf{v}_{j(0)}^{n+1/2}$ where $\mathbf{v}_{j(0)}^{n+1/2}$ is calculated by means of only the known field values at $t = t^n$.

The Maxwell equations in the finite-difference form assume the form

$$\mathbf{E}^{n+1} - \mathbf{E}^n = c \Delta t \nabla \times \mathbf{B}^{n+\alpha} - 4\pi \Delta t \mathbf{j}^{n+\gamma}, \quad (17)$$

$$\mathbf{B}^{n+1} - \mathbf{B}^n = -c \Delta t \nabla \times \mathbf{E}^{n+\alpha}. \quad (18)$$

In order to avoid the Courant condition that severely restricts the size of the time step Δt against the given space grid interval, we eliminate \mathbf{B}^{n+1} from Eqs.(17)(18) using the linear interpolation of the field quantity to the non-integer time level:

$$\mathbf{E}^{n+\alpha} = \alpha \mathbf{E}^{n+1} + (1 - \alpha) \mathbf{E}^n. \quad (19)$$

This procedure yields an equation governing the future electromagnetic field

$$\begin{aligned} [1 + (\alpha c \Delta t)^2 \nabla \times \nabla \times] \mathbf{E}^{n+1} &= [1 - \alpha(1 - \alpha)(c \Delta t)^2 \nabla \times \nabla \times] \mathbf{E}^n \\ &\quad + c \Delta t \nabla \times \mathbf{B}^n - 4\pi \Delta t \mathbf{j}^{n+\gamma}. \end{aligned} \quad (20)$$

In the above equation, all the terms except (1.) balance with each other for the electromagnetic part; by contrast, the (1.) terms and the current density contribute to determine the electrostatic field.

2.3 Directly-coupled field-particle equations

Since the implicitness parameters must be chosen as $\alpha, \gamma > \frac{1}{2}$, the current density in the equation (20) is unknown and needs to be predicted by some ways. This constitutes the key of the present algorithm which is done by expressing the current density directly

in terms of the electromagnetic field:

$$\mathbf{j}^{n+\gamma}(\mathbf{x}) = \sum_j e_j \mathbf{v}_j^{n+\gamma} S(\mathbf{x} - \tilde{\mathbf{x}}_j^{n+\gamma}) \quad (21)$$

$$= \sum_i e_i [\mathbf{v}_j^n + \gamma \Delta t \frac{e_i}{m_i} [\mathbf{E}^{n+\alpha} + \{ \frac{\mathbf{v}_j^n}{c} + \frac{\Delta t}{2} \frac{e_i}{m_i c} \left(\mathbf{E}^{n+\alpha} + \frac{\mathbf{v}_j^n}{c} \times \mathbf{B}^{n+\alpha} \right. \quad (22)$$

$$\left. + \frac{\Delta t}{2} \frac{e_i}{m_i c} \mathbf{E}^{n+\alpha} \times \mathbf{B}^{n+\alpha} \right) \} \times \frac{\mathbf{B}^{n+\alpha}}{1 + \left(\frac{\Delta t}{2} \frac{e_i B}{m_i c} \right)^2}] S(\mathbf{x} - \tilde{\mathbf{x}}_j^{n+\gamma}) \quad (23)$$

$$+ \sum_e (-e) [\{ v_{\parallel}^n + \gamma \Delta t \left(\frac{(-e)}{m_e} E_{\parallel}^{n+\alpha}(\tilde{\mathbf{x}}_j^{n+\gamma}) - \frac{\mu_j}{m_e} \nabla_{\parallel} B^{n+\alpha} \right) \} \mathbf{b}^{n+1/2} \quad (24)$$

$$+ \mathbf{v}_{\perp}^{n+\gamma}(\tilde{\mathbf{x}}_j^{n+\gamma})] S(\mathbf{x} - \tilde{\mathbf{x}}_j^{n+\gamma}). \quad (25)$$

The symbols \sum_i and \sum_e denote summations over the ions and electrons, respectively. Substitution of this expression into Eq.(20) with Eqs.(12)-(16) and (18) forms a closed set of the Courant-condition-free, implicit equations. These equations are named "directly-coupled field-particle equations".

The third and fourth equations of Maxwell equations, Eqs.(3)(4) are the conditions to determine the initial field and need not be used at $t > 0$ mathematically. However in reality, use of the space grids inevitably causes an assignment error to the longitudinal part of the current density. Therefore, correction to the electric field is required⁷⁾. This is done by deriving an correction equation to the longitudinal electric field:

$$\mathbf{E} = \tilde{\mathbf{E}} - \nabla \delta \varphi, \quad (26)$$

where \mathbf{E} is the true electric field, and $\tilde{\mathbf{E}}$ is the electric field before the correction (the solution to Eq.(20)). The Gauss equation (3) then yields an equation for $\delta \varphi$,

$$-\nabla^2 \delta \varphi = 4\pi \rho^{n+1} - \nabla \cdot \tilde{\mathbf{E}}^{n+1}. \quad (27)$$

Since the charge density at $t = t^{n+1}$ is not known beforehand in the implicit algorithm, the formula is used that expands the charge density⁸⁾ around the predicted position $\mathbf{x}_{(i)}^{n+1}$:

$$\begin{aligned} \rho^{n+1}(\mathbf{x}) &= \sum_j e_j S(\mathbf{x} - \mathbf{x}_j^{n+1}) \\ &= \sum_j e_j S(\mathbf{x} - \mathbf{x}_{(i)}^{n+1}) - \nabla \cdot \sum_j e_j \delta \mathbf{x}_j S(\mathbf{x} - \mathbf{x}_{(i)}^{n+1}). \end{aligned} \quad (28)$$

Here, $\delta \mathbf{x}_j = \mathbf{x}_j^{n+1} - \mathbf{x}_{(i)}^{n+1}$ with \mathbf{x}_j^{n+1} being the true position, and $\mathbf{x}_{(i)}^{n+1}$ the position calculated using $\tilde{\mathbf{E}}^{n+1}$ and \mathbf{B}^{n+1} . For example, the displacement for the ions becomes

$$\delta \mathbf{x}_j^{(i)} = -\frac{1}{2}\alpha(\Delta t)^2 \frac{e_i}{m_i} \left\{ \nabla \delta \varphi + \frac{1}{2} \Delta t \frac{e_i}{m_i c} \nabla \delta \varphi \times \mathbf{B}^{n+1} \right\} / \left[1 + \left(\frac{1}{2} \Delta t \frac{e_i B}{m_i c} \right)^2 \right]. \quad (29)$$

Thus, $\delta \mathbf{x}_j$ depends only on $\delta \varphi$ and Eqs.(27)(28) constitute the equations to determine the correction scalar potential field.

2.4 Miscellaneous

In the macroscale particle simulation, all the physical quantities are normalized by the four basic units, the length: c/ω_{pe} , time: ω_{pe}^{-1} , mass: m_e , charge: e , as

$$\hat{x} = \frac{x}{c/\omega_{pe}}, \quad \hat{t} = \omega_{pe} t, \quad \hat{m}_j = \frac{m_j}{m_e}, \quad \hat{e}_j = \frac{e_j}{e}. \quad (30)$$

Other quantities are normalized as combinations of these basic four units;

$$\hat{\mathbf{v}} = \frac{\mathbf{v}}{c}, \quad \hat{\omega} = \frac{\omega}{\omega_{pe}}, \quad \hat{\mathbf{E}} = \frac{e \mathbf{E}}{m_e c \omega_{pe}}, \quad \hat{\mathbf{B}} = \frac{e \mathbf{B}}{m_e c \omega_{pe}}. \quad (31)$$

Quantities with $(\hat{\cdot})$ are used in the simulation. This normalization is suitable for treating electromagnetic waves and instabilities. With this normalization, the constant in the field equations is transformed as $(4\pi) \rightarrow (1/n_0)$ and the light speed (c) disappears everywhere [n_0 : the average particle number density per cell].

Since the coupled equations are solved in the (x, y, k_z) space, the arrangement of the spatial grids needs to be specified for two-dimensional Cartesian coordinate space (Figure 1). Each component of the electromagnetic field and the source terms has its own grid system so that their spatial derivatives become centered with respect to the non-derivative terms. This is done by inspecting the Maxwell equations in the finite difference form. The proper combinations of the electromagnetic field in the coupled equations that share the same grid points are (E_x, B_y) and (E_y, B_x) ; E_z and B_z are defined on their own grids. With this choice, the accuracy of the spatial derivatives is kept to the second order.

Filtering of both the source terms in the coupled equations and the electromagnetic field acting on particles are required to reduce short wavelength errors associated

with the finite difference method. In terms of the (x, y) coordinate, the digital filtering technique known as "five-point smoothing" is done which is a combination of the three-point higher-mode filtering and the lower-mode boosting⁹⁾. The weight of this smoothing should be $(-\frac{1}{16}, \frac{4}{16}, \frac{10}{16}, \frac{4}{16}, -\frac{1}{16})$ for consecutive five points along one direction. At the system boundary (wall), proper boundary conditions must be imposed on each field quantity.

The supercomputers are generally equipped with the vectorization feature for the do-loop operations. This feature can be efficiently utilized even for the fast Fourier transform (FFT) in the multi-dimensional circumstances. The highest degree of vectorization is achieved for the FFT scheme if all the (x, y) components are Fourier-transformed simultaneously as a one-dimensional array in terms of the same k_z value.

It should be noted that Eq.(21) and (28) include summations over the product of the particle and field quantities which represent a coupling of the neighboring plasma elements through the electromagnetic field. These calculations are usually too expensive otherwise the following approximation is made use of for the coupling terms:

$$\begin{aligned} \sum_j e_j \mathbf{E}^{n+\alpha}(\mathbf{x}_j) S(\mathbf{x} - \mathbf{x}_j) &= \sum_j e_j \mathbf{E}^n S(\mathbf{x} - \mathbf{x}_j) + \alpha \sum_j e_j (\mathbf{E}^{n+1} - \mathbf{E}^n) S(\mathbf{x} - \mathbf{x}_j) \quad (32) \\ &\cong \sum_j e_j \mathbf{E}^n(\mathbf{x}_j) S(\mathbf{x} - \mathbf{x}_j) + \alpha \rho(\mathbf{x}) (\mathbf{E}^{n+1} - \mathbf{E}^n)(\mathbf{x}). \quad (33) \end{aligned}$$

The linear interpolation (19) is used in the first line and $\rho(\mathbf{x}) = \sum_j e_j S(\mathbf{x} - \mathbf{x}_j)$. The summations through the particle list are thus separated from the iteration cycle of the coupled field-particle equations. Since the major contribution is contained in the first term of (33) whose calculation is done "accurately", this approximation is considered to be quite acceptable. This point has been verified numerically³⁾. Analytic and numerical proof of the macroscale particle simulation in general is found in Reference [3].

There are several remarks before closing this technical section. First, exactly identical expressions must be used in the particle movers and the corresponding parts in the directly-coupled field-particle equations. Violation to this rule always leads to a rapid blowup of the code. Secondly, for the proper tracking of the cyclotron motion

the complete time-centered integration scheme should be used in the Lorentz term of the particle mover in order to avoid a fictitious acceleration of the ions. Moreover, in the initial transient state, give the electron $\mathbf{E} \times \mathbf{B}$ term somewhat less than the correct value; this enables us to avoid an overreaction of this "passive" term.

Next, the time step Δt should be chosen as: $\omega_\alpha \Delta t \leq 0.4$ for proper ion orbit tracking, and $k_{\parallel, \max} v_{\parallel} \Delta t \ll 1$ to correctly resolve the wave with the wavelength $\lambda = 2\pi/k_{\parallel, \max}$ (Short waves are usually eliminated by the digital filtering). Another limitation to the time step arises from the possible discrepancy between the true particle position $\mathbf{x}_j^{n+\gamma}$ and the predicted position $\tilde{\mathbf{x}}_j^{n+\gamma}$ which is used to evaluate the field acting on the super-particles (see just below Eq.(16)). The difference of the two positions for the electrons, for example, is written as

$$\delta \mathbf{x}_D \equiv \mathbf{x}_j^{n+\gamma} - \tilde{\mathbf{x}}_j^{n+\gamma} = \gamma \Delta t (\mathbf{v}_j^{n+1/2} - \mathbf{v}_{j(0)}^{n+1/2}) \quad (34)$$

$$\cong \frac{1}{2} \gamma (\Delta t)^2 \frac{(-e)}{m_e} (E_{\parallel}^{n+\alpha} - E_{\parallel}^n) + \gamma \Delta t (\mathbf{v}_{\perp}^{n+\gamma} - \mathbf{v}_{\perp}^n). \quad (35)$$

The accuracy condition may be given by

$$\frac{\delta \mathbf{x}_D}{\Delta x} \cong \frac{\Delta t}{\Delta x} \left\{ \frac{1}{2} \gamma \Delta t \frac{(-e)}{m_e} (E_{\parallel}^{n+\alpha} - E_{\parallel}^n) + \gamma (\mathbf{v}_{\perp}^{n+\gamma} - \mathbf{v}_{\perp}^n) \right\} \ll 1. \quad (36)$$

These electric fields include both the physical component and the noises due to particle discreteness. For the monochromatic sinusoidal wave of $E_{\parallel}^n \sim e^{i\omega n \Delta t}$, we have

$$E_{\parallel}^{n+\alpha} - E_{\parallel}^n \approx i\alpha\omega\Delta t E_{\parallel}^n. \quad (37)$$

Since $\alpha\omega\Delta t \ll 1$ for the resolved modes in the macroscale particle simulation, $|\delta \mathbf{x}_{D,\tau}|$ can be made small enough compared with the cell size. However, without any precautions the discrepancy due to the noise field could be as large as

$$\delta \mathbf{x}_{D,n} \approx \frac{1}{2} \gamma (\Delta t)^2 \frac{(-e)}{m_e} \mathbf{E}_{noise} + \gamma \Delta t \mathbf{v}_{\perp, noise}. \quad (38)$$

This can be apparently larger than the former value if the noise level is comparable to the signal level. Therefore, in order to make the difference $|\delta \mathbf{x}_D|$ small compared with the cell size, more number of particles is required to reduce the noise level, thereby increasing the size of the time step Δt .

3 Application 1: Alfven Ion Cyclotron Instability

As the first physics application of the macroscale particle code, one-dimensional simulation results are described where the Alfven-ion-cyclotron (AIC) wave is driven unstable by the ion temperature anisotropy.

The Alfven-ion-cyclotron instability was investigated by many authors analytically¹⁰⁾ and numerically¹¹⁻¹³⁾. The dispersion relation of the AIC wave that propagates parallel to the ambient magnetic field is given by

$$\omega^2 - c^2 k^2 + \omega_{pe}^2 \left(\frac{\omega}{kv_e} \right) Z(\xi_e) + \omega_{pi}^2 \left(\frac{\omega}{kv_{i\parallel}} \right) Z(\xi_i) \quad (39)$$

$$- \omega_{pi}^2 \left(1 - \frac{T_{i\perp}}{T_{i\parallel}} \right) [1 + \xi_i Z(\xi_i)] = 0, \quad (40)$$

where $\xi_e = (\omega \pm \omega_{ce})/kv_e$, $\xi_i = (\omega \pm \omega_{ci})/kv_{i\parallel}$ with ω_{ce} , ω_{ci} being the electron and ion cyclotron frequencies and v_e , v_i the thermal speeds of the electrons and ions, respectively. The perpendicular temperature of the ions, $T_{i\perp}$ is defined by

$$T_{i\perp} = 2\pi \int_{-\infty}^{\infty} dv_{\parallel} \int_0^{\infty} dv_{\perp} v_{\perp} \left(\frac{1}{2} m_i v_{\perp}^2 \right) f_i(v_{\parallel}, v_{\perp}). \quad (41)$$

Here $f_i(v_{\parallel}, v_{\perp})$ is the velocity distribution function of the ions. When the perpendicular temperature is greater than the parallel one, *i.e.*, $(T_{\perp}/T_{\parallel})_i > 1$, then the AIC instability is excited. The typical frequency in the large anisotropy limit is $\omega \sim \omega_{ci}$, the growth rate $\gamma \sim (\beta_{\perp}/2)^{1/2}$ and the wavenumber $ck/\omega_{pi} \sim 1$. The aforementioned dispersion relation reveals that any ion velocity distribution with the same temperature anisotropy is equivalent for the AIC instability¹⁰⁾. The spectrum width of the unstable wavenumber and the maximum growth rate are the increasing functions of the $(T_{\perp}/T_{\parallel})_i$ ratio and the ion beta value.

In the past the so-called hybrid particle code used to be the major tool of simulating the AIC instability. In the hybrid simulation the electrons were treated as the massless species and the electrostatic part of the electric field was essentially omitted^{12,13)}. By contrast, in the present macroscale particle simulation the electrons are treated as the particle species along the magnetic field line; only the $E \times B$ drift term is included

in this application in the perpendicular direction. Before starting the simulation, the initial velocities are given to the ions and electrons so that each of the species follows the Maxwell distribution at rest. The temperature anisotropy of $(T_{\perp}/T_{\parallel})_i = 5 - 20$ is given to the ions. The other parameters chosen are the system size $L_z = 120c/\omega_{pe}$, the electron thermal speed $v_e/c = 0.2$, the temperature ratio $T_{i\parallel}/T_e = 1$, and the ambient magnetic field strength $\omega_{ce}/\omega_{pe} = 0.7$ which corresponds to $\omega_{ci}/\omega_{pi} = 0.1$ for $m_i/m_e = 50$ case. (Note that the electron cyclotron frequency does not appear in the present simulation algorithm.) The parallel beta value is then $\beta_{i\parallel} \sim 8 \times 10^{-2}$. The number of the cells in the z -direction is 128, the number of particles for each species is 12,800 and the time step is $\omega_{pe}\Delta t = 20$. The quiet start technique of loading four particles in pair is used to minimize the initial noise.

The time histories of the perturbed magnetic and electric field energies are shown for $(T_{\perp}/T_{\parallel})_i = 20$ case in Fig 2(a) and (b), respectively. The magnetic field energy grows exponentially from the initial low noise level and saturates around $\omega_{ci}t \sim 40$. For the electric field the initial noise level is dominated by the electrostatic field, and the electromagnetic instability appears to emerge abruptly above the noise level at $\omega_{ci}t \sim 30$. The growth rate is measured to be $\gamma/\omega_{ci} \sim 0.44$ for the mode three with $ck/\omega_{pi} \sim 1.1$ which is in agreement with the linear theory of the AIC instability.

The time history of the ion temperature anisotropy, $(T_{\perp}/T_{\parallel})_i$, is shown in Fig.2(c). When the intensity of the perturbed magnetic field reaches a certain level, *i.e.*, $\langle \delta B^2 \rangle / 8\pi nT_i \sim 0.2$, the temperature anisotropy begins to decrease. (This decrease begins much earlier and occurs more gradually if the quiet start technique is not used.) This process occurs relatively in a short time scale, $13\omega_{ci}^{-1}$. The final value of the anisotropy, $(T_{\perp}/T_{\parallel})_i \cong 2$ is found to be almost independent of the initial temperature anisotropies; the measured final anisotropies are 2.0, 1.8 and 2.3 for the initial anisotropies of 5, 10 and 20, respectively. The run with the smaller initial anisotropy $(T_{\perp}/T_{\parallel})_{i0} = 5$ has been made until $\omega_{ci}t \sim 500$. For the $(T_{\perp}/T_{\parallel})_{i0} = 20$ case, another run is performed with a longer system size $L_z = 240c/\omega_{pe}$ because the longer wavelength modes are still expected to be unstable in the later stage with subdued anisotropy. The run is

continued up to $\omega_{ci}t \sim 84$ but the anisotropy completely ceases to decrease at $\omega_{ci}t \sim 70$ and the final value of the anisotropy is measured to be $(T_{\perp}/T_{\parallel})_i = 1.9$.

The three components of the electric field at $\omega_{ci}t = 42$ are plotted in Fig.3. We can see somewhat deformed sinusoidal wave of the mode number three. The electromagnetic components associated with the AIC instability, E_x and E_y , are already larger than the electrostatic component E_z at this stage. The mode number of the most unstable wave, four in the middle of the linear stage, has decreased to three at the beginning of the nonlinear stage of Fig.3.

A series of ion scatter plots in the (v_z, v_{\perp}) , (z, v_z) and (z, ψ) spaces are shown from top to bottom in Fig.4, respectively. Here, $\psi = \tan^{-1}(v_y/v_x)$ is the phase angle of the perpendicular velocity of the ions. The ions receive a remarkable pitch angle scattering during $\omega_{ci}t \sim 30 - 40$. This is most clearly seen as the change in the (v_z, v_{\perp}) space distribution from the needle-like distribution into a more isotropic round-shaped one at later times. This phenomenon has been observed as the decrease in the temperature anisotropy in Fig.2(c).

More interesting observation is that the ions and electrons are highly modulated both in the velocity space and the configuration space. The ion modulation in the phase space (z, ψ) at the end of the linear stage $\omega_{ci}t \sim 42$ (Fig.4(c)) is in-phase with the magnetic perturbation of Fig.4(d) and by 90 degrees out-of-phase with the electric field. This modulation of the velocity phase angle in response to the magnetic perturbation was also reported by the hybrid simulation¹²⁾. However, the density modulation in the configuration space, which is shown in Fig.5 at $\omega_{ci}t \sim 42$ and 56, develops only after the occurrence of the velocity modulation. This phenomenon has newly been noticed in the present macroscale particle simulation.

The modulation of the velocity phase angle is just a consequence of the AIC instability which occurs linearly in response to the wave perturbation. On the other hand, the modulation in the configuration space, *i.e.* the density perturbation, occurs following the pitch angle scattering process. In other words, the density perturbation

occurs in the nonlinear stage of the instability. The number of the density peaks is equal to twice the mode number of the dominant AIC magnetic perturbation. A good spatial correlation is found between the ion density modulation and the intensity of the magnetic field $|B|^2(z)$; the ion density is higher where the magnetic field intensity is lower, and vice versa. The electrons suffer from nearly the same modulations both in the velocity space and the configuration space. Therefore, the density perturbation may be attributed to the electromagnetic ponderomotive force $\langle \delta \mathbf{E} \times \delta \mathbf{B} \rangle (z)$ due to the finite amplitude AIC waves.

The overall results of the AIC instability have agreed well between the present macroscale simulation and the past hybrid simulation. The efficiency of the computation is twice better for the hybrid simulation in one-dimensional case. However, many of us found in the past that the hybrid simulation abruptly ended up with a blowup of the code in the middle of the nonlinear stage of the instability. The macroscale simulation could continue far beyond this point and is considered to be more viable than the hybrid simulation.

4 Application 2: Kink Instability of Peaked Density Beam

The full-implicit algorithm of the macroscale particle simulation described in Sec.2 is now applied to kink instability in the three-dimensional space which occurs to the current-carrying ion beam with an inhomogeneous density profile. The simulation of the Alfvén critical current and kink instability was carried out several years ago against the relativistic electron beam by using the semi-implicit version of the macroscale particle code⁶⁾. Here we use the full-implicit version of the macroscale particle code. The latter has been found to be at least ten times more efficient than the former for the same physics problem.

The simulation is performed in the three-dimensional space (x, y, z, v_x, v_y, v_z) ; par-

ticles move in this six-dimensional space. The electromagnetic field is solved in the real (configuration) space for x and y coordinates and in the Fourier space for the periodic z -coordinate toward which the ambient magnetic field is applied. This type of the field solver is favorable for treating inhomogeneous density, wall-bound plasmas. Moreover, this code is to be expandable without any major changes to non-square poloidal cross section and/or torus geometries such as tokamaks and stellarators.

The system size of the simulation is $L_x = L_y = 40c/\omega_{pe}$ and $L_z = 400c/\omega_{pe}$ with $27 \times 27 \times 32$ grids in each direction. The electrons and ions have a bell-shaped density profile $n_0(r) \sim 1/\cosh^2(r/L_n)$ which is peaked at the center of the (x, y) plane. The width of the density profile is $L_n = 15c/\omega_{pe}$. An initial drift along the ambient magnetic field is given to the ions to create the current-carrying beam. The initial drift speed v_{dz} is chosen so that the safety factor at the radial distance $r = L_n$ becomes $q(r) \approx 0.5$. Other physical parameters are: the ambient magnetic field strength $\omega_{ce}/\omega_{pe} = 1$, the temperature ratio $T_e/T_i = 1$ and the electron beta value $\beta_e = 0.09$. (Note that the magnetic field strength is given by the ratio ω_{ce}/ω_{pe} .) The mass ratio is $m_i/m_e = 50$ and the time step is $\omega_{pe}\Delta t = 20$. This corresponds to $\omega_{ci}\Delta t = 0.4$ under the given parameters.

In the simulation run a helical distortion of the ion beam becomes apparent from $\omega_{ci}t \sim 40$. The distortion has the mode number $m/n=1/2$ in the early stage. The displacement due to this distortion takes a maximum value around $\omega_{ci}t \sim 130$ and stays at this level thereafter. Fig.6 is the bird's-eye view plot of the ion distribution in the (x, y, z) space. At $\omega_{ci}t \sim 140$, the $m/n=1/1$ helical distortion is clearly observed with the $m/n=1/2$ mode superimposed on it. Almost the same helical distortion in the spatial phase and the amplitude is observed for the electrons. This fact implies an occurrence of the helical distortion of the magnetic field structure.

The poloidal magnetic field is plotted in Fig.7 for the four poloidal cross sections with the equal toroidal separation. The helical shift of the magnetic axis is found as expected, although the average position of the axis has moved somewhat above $x = \frac{1}{2}L_x$. For the present run the poloidal Alfvén time is calculated to be $\tau_A =$

$L_x/v_{Ap} \sim 11\omega_{ci}^{-1}$ where $v_{Ap} = B_p/(4\pi m_i n)^{1/2}$. Since the above helical distortion occurs in a few poloidal Alfvén times, it is considered to be an ideal magnetohydrodynamic phenomenon - the ideal kink instability¹⁴⁾.

5 Conclusion

In this paper, the advanced implicit algorithm has been presented that is to be applied to studies of finite beta kinetic and inhomogeneous plasmas in large space and time scales. The keys of the code are the introduction of the slightly backward time-decentered scheme, use of the directly-coupled field-particle equations and the guiding center approximation of the electron perpendicular motion. The code has been successfully implemented for studies of three-dimensional, inhomogeneous and magnetized plasmas.

As a verification of the code, two physics applications have been shown in Sec.3 and 4. In the first application, the Alfvén-ion-cyclotron instability has been shown to be excited by the initially given ion temperature anisotropy. The ions suffer from the pitch-angle scattering and strong modulations both in the phase and configuration spaces. The anisotropy relaxes to $(T_{\perp}/T_{\parallel}) \approx 2$ irrespective of the initial anisotropies. In the second application, the current-carrying ion beam with the inhomogeneous density profile has been shown to undergo the helical kink instability in the ideal magnetohydrodynamic time scale.

As has been described in this paper, the macroscale particle simulation has enabled us the studies of kinetic plasmas in large space and time scales that were not possible by either the traditional particle or magnetohydrodynamic simulation methods. The efficiency of the macroscale particle simulation is comparable (about one half) with the hybrid particle simulation. But the macroscale simulation retains physical processes concerning the electrons which are completely ignored in the hybrid simulation. Moreover, the macroscale particle simulation is stable even when the hybrid simulation fails

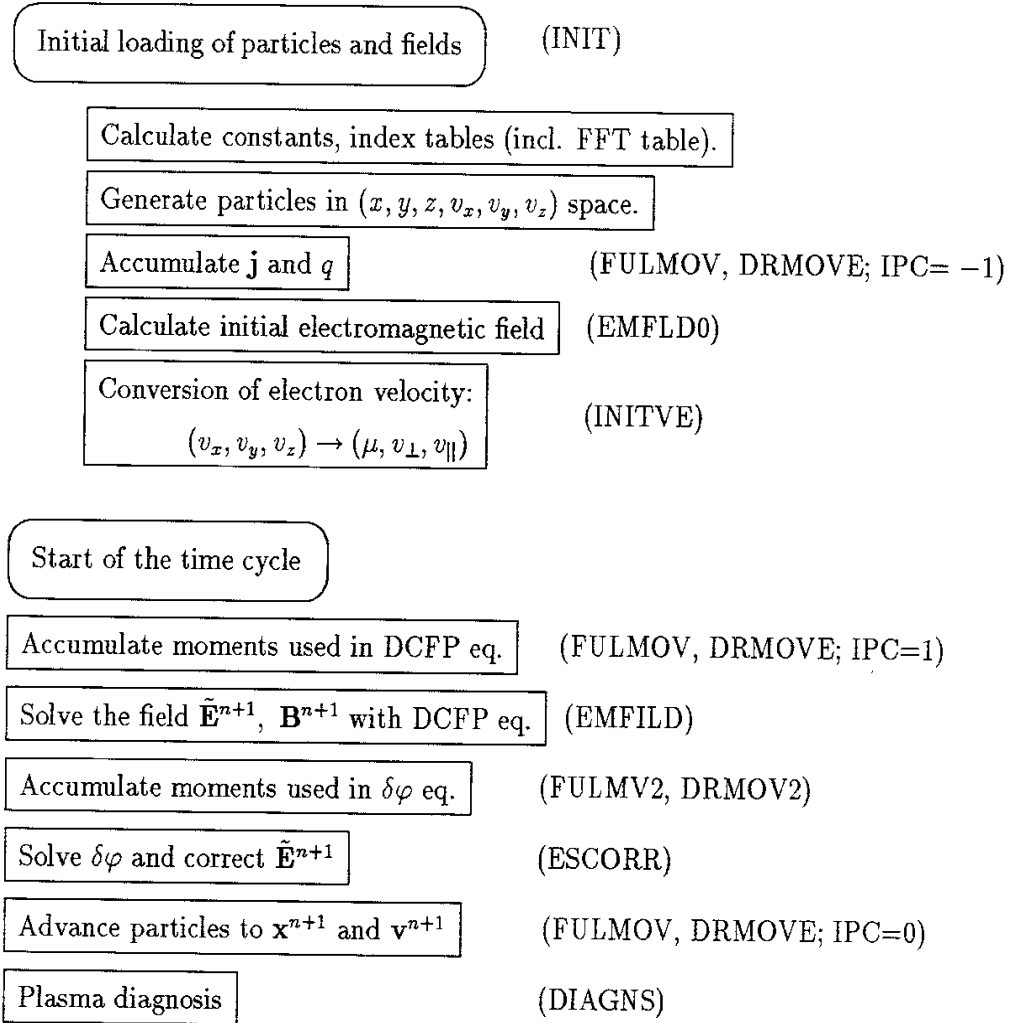
numerically.

In the future several extensions are possible. The extension to the torus geometry (r, z, ϕ) is necessary to study stability and transport processes occurring in tokamaks and stellarators. Use of the guiding-center approximation for the perpendicular motion of the ions is also suggested to perform simulations with $\omega_{ci}\Delta t \gg 1$. To deal with the plasma with magnetic field nulls, the macroscale particle code with full-particle species is required. (Its coding is simpler than the present one.) But the condition $\omega_{ce}^{Max}\Delta t \leq 0.4$ may limit its simulation parameters. Alternatively, paste up of the electron guiding-center code ($B \neq 0$) and the full-particle species code may be possible.

Finally, in order to make the code really helpful for the study of transport processes in magnetized plasmas, it is necessary to know the nature of numerical noises and to find out the noise reduction technique associated with the particle discreteness. Intensive research efforts are now being exploited in this area (see Sec.2.4). In the near future, the macroscale particle simulation code will be modified to include the torus effects and/or the inter-particle collision that is too microscopic to take into the macroscopic regime of our interest.

Appendix: Flow Chart of MACROS Code

A series of subroutines that constitute one time cycle of the macroscale particle simulation is shown here. The top part of the flow chart shows the initial loading of the particles and the electromagnetic field. The names in parentheses on the right are the subroutines for each procedure. The bottom part shows one time cycle of the simulation.



IF $t < t_F$, and $(\text{ctime}) < (\text{ctime})_F$, GOTO
Start of the time cycle

END

Acknowledgement

One of the author (M.T.) thanks Dr.C.Z.Cheng for discussion about handling of the diamagnetic terms and he thanks the staffs at the Theory and Computer Simulation Research Center of Institute for Fusion Science for general discussions.

References

1. J.U.Brackbill and D.W.Forslund, J.Comput.Phys., 46, 271 (1982);
D.W.Forslund and J.U.Brackbill, Phys.Rev.Lett., 48, 1614 (1982).
2. H.X.Vu and J.U.Brackbill, Comput.Phys.Comm., submitted (1991).
3. M.Tanaka, J.Comput.Phys., 79, 209 (1988).
4. J.F.Federici, W.W.Lee and W.M.Tang, Phys.Fluids, 30, 425 (1987).
5. M.Tanaka, T.Sato and A.Hasegawa, Phys. Fluids, B1, 325 (1989).
6. M.Tanaka and T.Sato, Phys.Fluids, 29, 3823 (1986).
7. A.B.Langdon and B.F.Lasinski, Methods in Comput. Phys., 16, 327 (1976).
8. A.B.Langdon, J.Comput.Phys., 30, 202 (1979).
9. C.K.Birdsall and A.B.Langdon, Plasma physics via computer simulation, McGraw-Hill (1985).
10. R.C.Davidson and J.M.Ogden, Phys.Fluids, 18, 1045 (1975).
11. M.Tanaka, C.C.Goodrich, D.Winske and K.Papadopoulos, J.Geophys.Res., 88, 3046 (1983).
12. M.Tanaka, J.Geophys.Res., 90, 6459 (1985).
13. Y.Omura, H.Matsumoto, R.Gendrin and M.Abdalla, J.Geophys.Res., 90, 8281 (1985).
14. G.Bateman, MHD instabilities (MIT Press, 1978).

Table

Table 1. Characteristics of Macroscale Particle Simulation Code

<ul style="list-style-type: none"> • Large space and time scales: $\omega_{pe}\Delta t \gg 1$, $\omega_{ce}\Delta t \gg 1$, and $\Delta x/(c/\omega_{pe}) \geq 1$ • Fully electromagnetic. • Multi-dimensions in any geometry (Cartesian, cylinder, torus). • Inhomogeneous density profile and arbitrary magnetic field structure. • Fully kinetic: <ul style="list-style-type: none"> ions: 3-D motion electrons: parallel direction \rightarrow 1-D motion with $(-\mu\nabla_{\parallel}B)$ force. perpendicular direction \rightarrow guiding-center approximation $(\mathbf{E} \times \mathbf{B}, \nabla B, \text{curvature drifts})$ 	\rightarrow <ul style="list-style-type: none"> Resonance effects (Landau, cyclotron resonances) Orbit effects: finite Larmor radius effects diamagnetic current banana orbit... Longitudinal particle transport 	} included.
--	--	-------------

Figure Captions

Figure 1. Field grid system in the two-dimensional Cartesian space. Each component of the electromagnetic field is calculated on the points of its own grid system.

Figure 2. Time histories of the perturbed magnetic and electric field energies (in logarithmic scales) and the temperature anisotropy $(T_{\perp}/T_{\parallel})_i$ for the AIC instability of $(T_{\perp}/T_{\parallel})_{i0} = 20$.

Figure 3. The three components of the electric field, E_x , E_y and E_z at $\omega_{ci}t = 42$.

Figure 4. Scatter plots of the ions in the (v_z, v_{\perp}) , (z, v_z) and (z, ψ) spaces (from top to bottom, respectively) for $\omega_{ci}t = 0, 42$ and 56 [$\psi = \tan^{-1}(v_y/v_x)$]. The phase angle of the magnetic perturbation, $\tan^{-1}(B_y/B_x)$ is shown against the z coordinate in the bottom row.

Figure 5. The spatial profiles of the ion and electron densities, and the intensity of the magnetic field $|B^2|$ at (a) $\omega_{ci}t = 42$ and (b) $\omega_{ci}t = 56$.

Figure 6. Occurrence of the helical kink instability against the ion beam with the peaked density profile in the three-dimensional magnetized plasma where the spatial distribution of the ions is shown at $\omega_{ci}t \sim 0$ and 140 .

Figure 7. The magnetic field of $\omega_{ci}t \sim 140$ in the poloidal cross sections at $z = 0, \frac{1}{4}L_x, \frac{1}{2}L_x$ and $\frac{3}{4}L_x$.

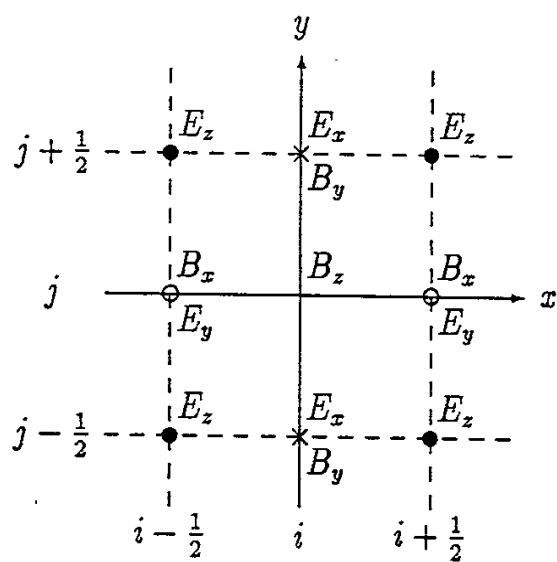


Figure 1.

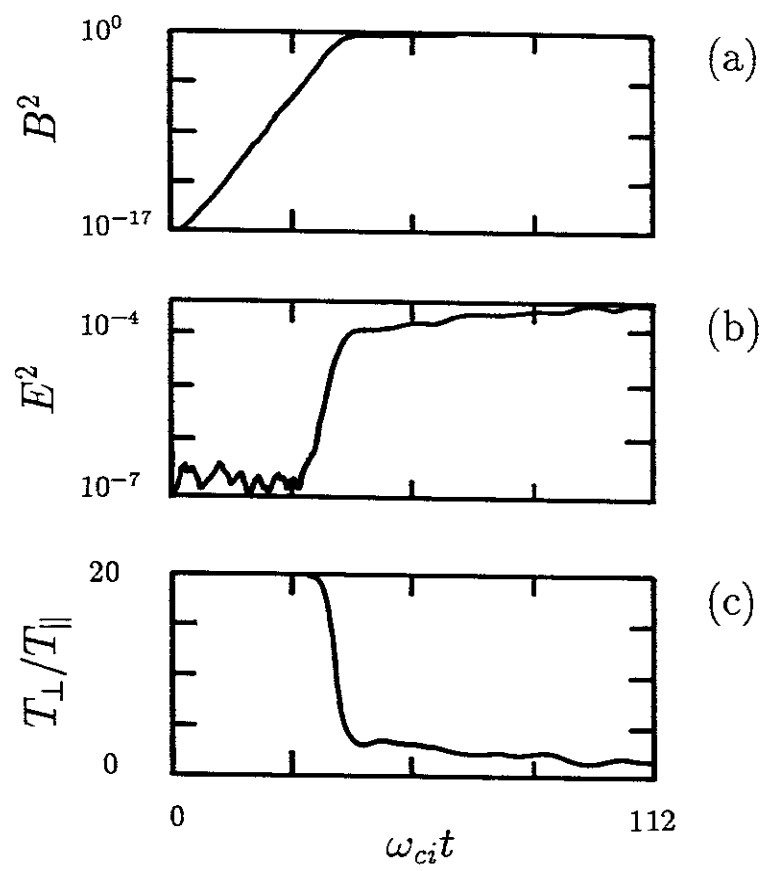


Figure 2.

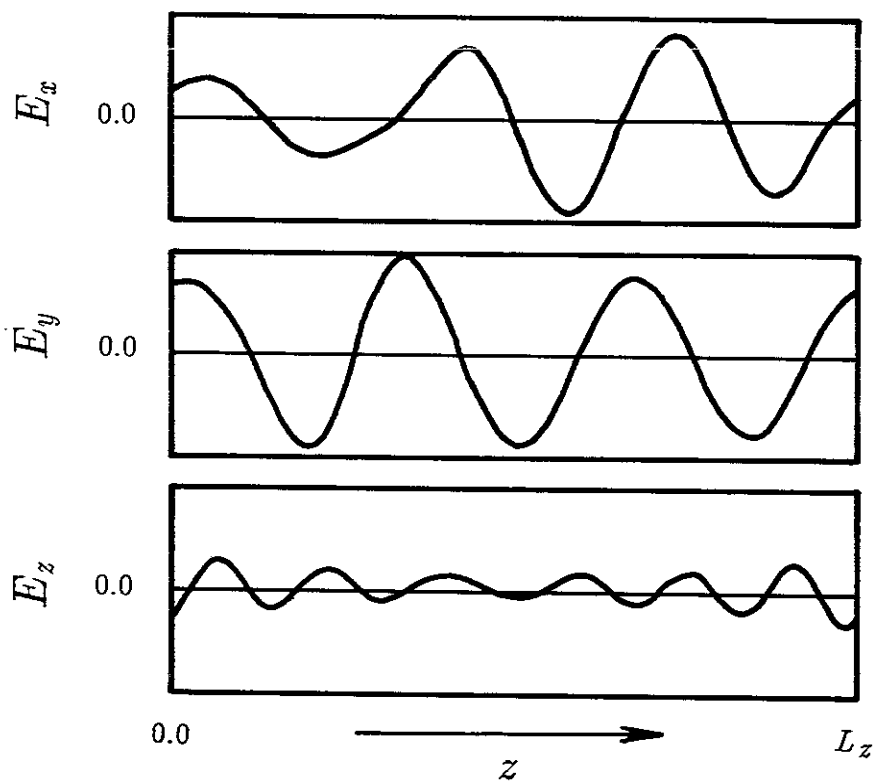


Figure 3.

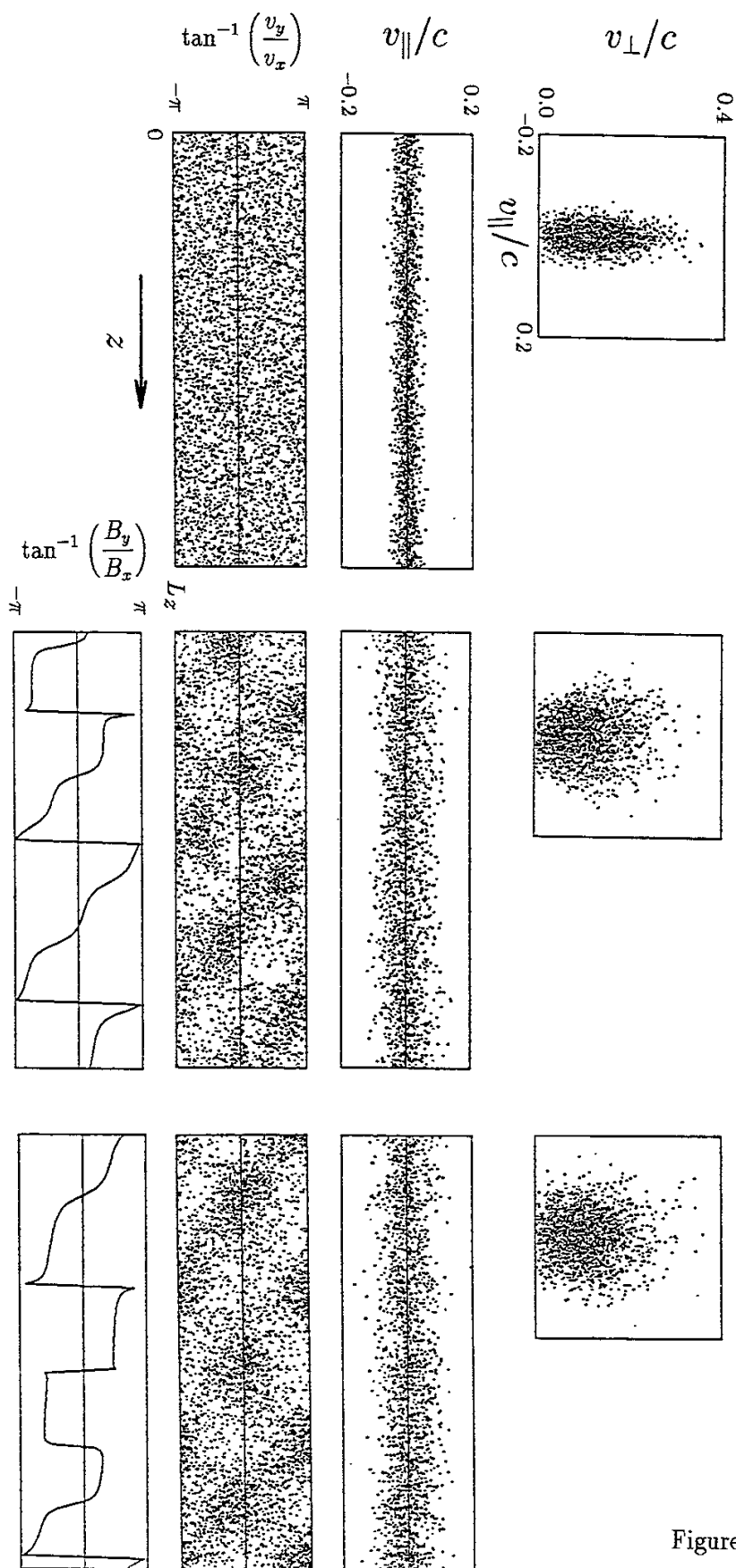


Figure 4.

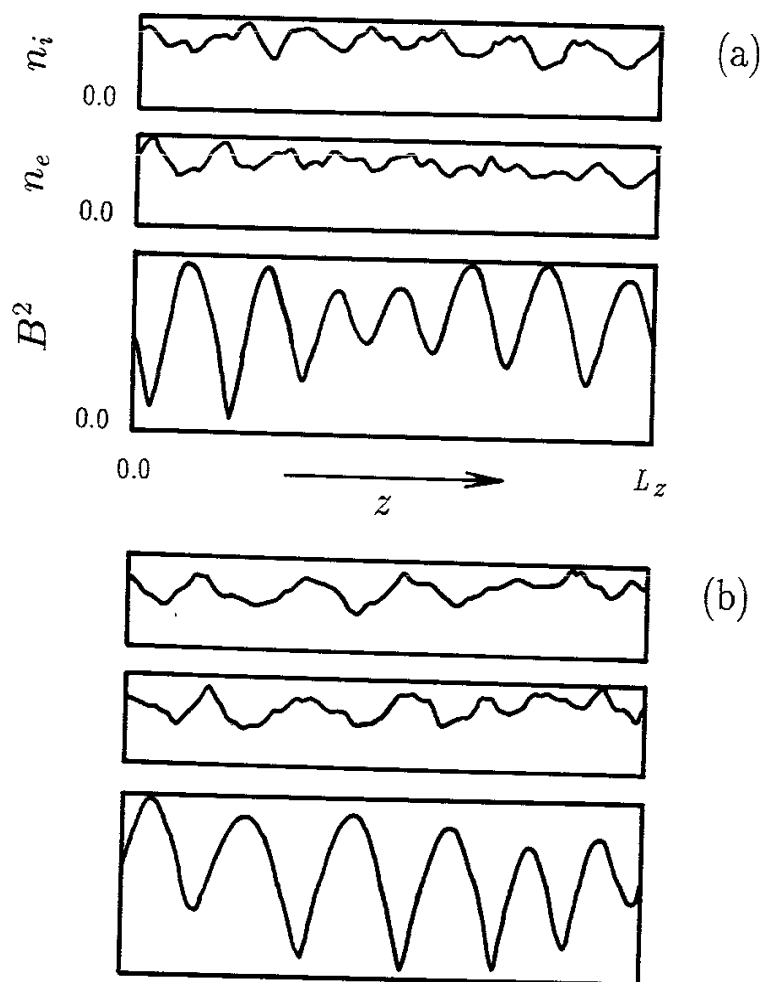


Figure 5.

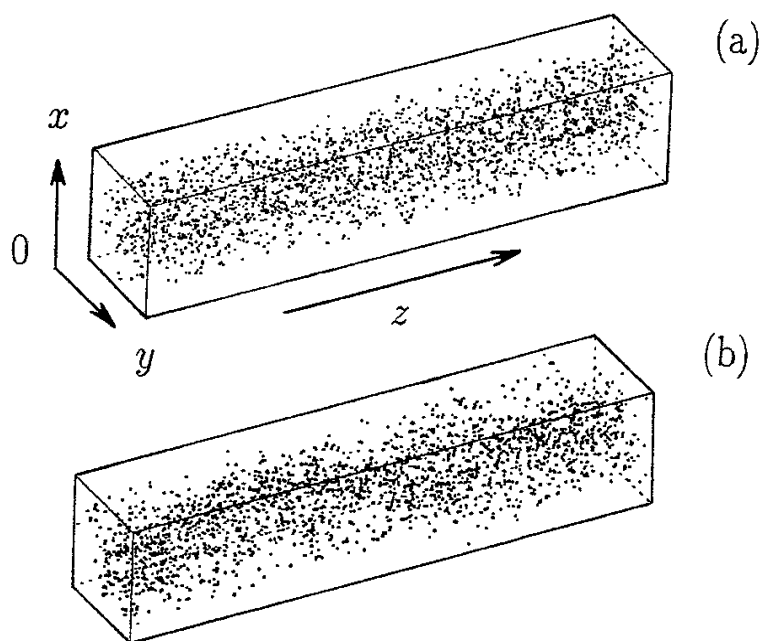


Figure 6.

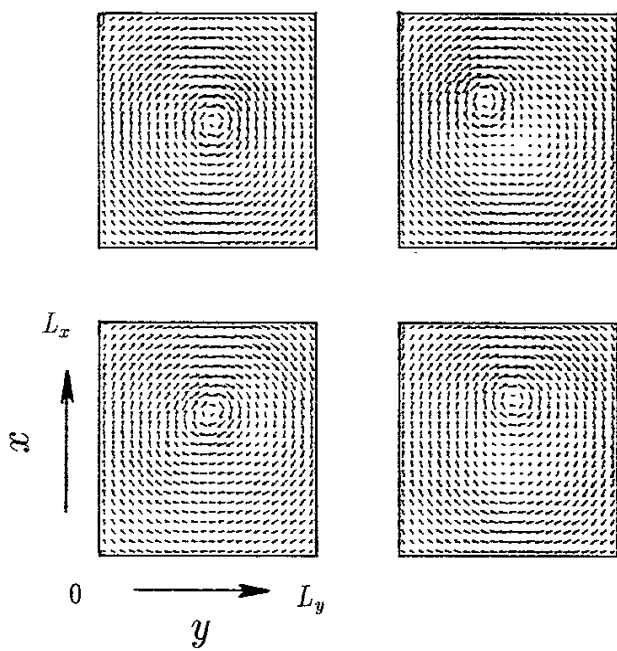


Figure 7

Recen Issues of NIFS Series

- NIFS-40 K. Toi, Y. Hamada, K. Kawahata, T. Watari, A. Ando, K. Ida, S. Morita, R. Kumazawa, Y. Oka, K. Masai, M. Sakamoto, K. Adati, R. Akiyama, S. Hidekuma, S. Hirokura, O. Kaneko, A. Karita, T. Kawamoto, Y. Kawasumi, M. Kojima, T. Kuroda, K. Narihara, Y. Ogawa, K. Ohkubo, S. Okajima, T. Ozaki, M. Sasao, K. Sato, K.N. Sato, T. Seki, F. Shimpō, H. Takahashi, S. Tanahashi, Y. Taniguchi and T. Tsuzuki, *Study of Limiter H- and IOC- Modes by Control of Edge Magnetic Shear and Gas Puffing in the JIPP T-IIU Tokamak*; Sep. 1990
- NIFS-41 K. Ida, K. Itoh, S.-I. Itoh, S. Hidekuma and JIPP T-IIU & CHS Group, *Comparison of Toroidal/Poloidal Rotation in CHS Heliotron/Torsatron and JIPP T-IIU Tokamak*; Sep. 1990
- NIFS-42 T. Watari, R. Kumazawa, T. Seki, A. Ando, Y. Oka, O. Kaneko, K. Adati, R. Ando, T. Aoki, R. Akiyama, Y. Hamada, S. Hidekuma, S. Hirokura, E. Kako, A. Karita, K. Kawahata, T. Kawamoto, Y. Kawasumi, S. Kitagawa, Y. Kitoh, M. Kojima, T. Kuroda, K. Masai, S. Morita, K. Narihara, Y. Ogawa, K. Ohkubo, S. Okajima, T. Ozaki, M. Sakamoto, M. Sasao, K. Sato, K.N. Sato, F. Shinbo, H. Takahashi, S. Tanahashi, Y. Taniguchi, K. Toi, T. Tsuzuki, Y. Takase, K. Yoshioka, S. Kinoshita, M. Abe, H. Fukumoto, K. Takeuchi, T. Okazaki and M. Ohtuka, *Application of Intermediate Frequency Range Fast Wave to JIPP T-IIU and HT-2 Plasma*; Sep. 1990
- NIFS-43 K. Yamazaki, N. Ohyabu, M. Okamoto, T. Amano, J. Todoroki, Y. Ogawa, N. Nakajima, H. Akao, M. Asao, J. Fujita, Y. Hamada, T. Hayashi, T. Kamimura, H. Kaneko, T. Kuroda, S. Morimoto, N. Noda, T. Obiki, H. Sanuki, T. Sato, T. Satō, M. Wakatani, T. Watanabe, J. Yamamoto, O. Motojima, M. Fujiwara, A. Iiyoshi and LHD Design Group, *Physics Studies on Helical Confinement Configurations with $l=2$ Continuous Coil Systems*; Sep. 1990
- NIFS-44 T. Hayashi, A. Takei, N. Ohyabu, T. Sato, M. Wakatani, H. Sugama, M. Yagi, K. Watanabe, B.G. Hong and W. Horton, *Equilibrium Beta Limit and Anomalous Transport Studies of Helical Systems*; Sep. 1990
- NIFS-45 R. Horiuchi, T. Sato, and M. Tanaka, *Three-Dimensional Particle Simulation Study on Stabilization of the FRC Tilting Instability*; Sep. 1990
- NIFS-46 K. Kusano, T. Tamano and T. Sato, *Simulation Study of Nonlinear Dynamics in Reversed-Field Pinch Configuration*; Sep. 1990
- NIFS-47 Yoshi H. Ichikawa, *Solitons and Chaos in Plasma*; Sep. 1990

- NIFS-48 T.Seki, R.Kumazawa, Y.Takase, A.Fukuyama, T.Watari, A.Ando, Y.Oka, O.Kaneko, K.Adachi, R.Akiyama, R.Ando, T.Aoki, Y.Hamada, S.Hidekuma, S.Hirokura, K.Iida, K.Itoh, S.-I.Itoh, E.Kako, A. Karita, K.Kawahata, T.Kawamoto, Y.Kawasumi, S.Kitagawa, Y.Kitoh, M.Kojima, T.Kuroda, K.Masai, S.Morita, K.Narihara, Y.Ogawa, K.Ohkubo, S.Okajima, T.Ozaki, M.Sakamoto, M.Sasao, K.Sato, K.N.Sato, F.Shinbo, H.Takahashi, S.Tanahashi, Y.Taniguchi, K.Toi and T.Tsuzuki, *Application of Intermediate Frequency Range Fast Wave to JIPP T-IIU Plasma*; Sep.1990
- NIFS-49 A.Kageyama, K.Watanabe and T.Sato, *Global Simulation of the Magnetosphere with a Long Tail: The Formation and Ejection of Plasmoids*; Sep.1990
- NIFS-50 S.Koide, *3-Dimensional Simulation of Dynamo Effect of Reversed Field Pinch*; Sep. 1990
- NIFS-51 O.Motojima, K. Akaishi, M.Asao, K.Fujii, J.Fujita, T.Hino, Y.Hamada, H.Kaneko, S.Kitagawa, Y.Kubota, T.Kuroda, T.Mito, S.Morimoto, N.Noda, Y.Ogawa, I.Ohtake, N.Ohyabu, A.Sagara, T. Satow, K.Takahata, M.Takeo, S.Tanahashi, T.Tsuzuki, S.Yamada, J.Yamamoto, K.Yamazaki, N.Yanagi, H.Yonezu, M.Fujiwara, A.Iiyoshi and LHD Design Group, *Engineering Design Study of Superconducting Large Helical Device*; Sep. 1990
- NIFS-52 T.Sato, R.Horiuchi, K. Watanabe, T. Hayashi and K.Kusano, *Self-Organizing Magnetohydrodynamic Plasma*; Sep. 1990
- NIFS-53 M.Okamoto and N.Nakajima, *Bootstrap Currents in Stellarators and Tokamaks*; Sep. 1990
- NIFS-54 K.Itoh and S.-I.Itoh, *Peaked-Density Profile Mode and Improved Confinement in Helical Systems*; Oct. 1990
- NIFS-55 Y.Ueda, T.Enomoto and H.B.Stewart, *Chaotic Transients and Fractal Structures Governing Coupled Swing Dynamics*; Oct. 1990
- NIFS-56 H.B.Stewart and Y.Ueda, *Catastrophes with Indeterminate Outcome*; Oct. 1990
- NIFS-57 S.-I.Itoh, H.Maeda and Y.Miura, *Improved Modes and the Evaluation of Confinement Improvement*; Oct. 1990
- NIFS-58 H.Maeda and S.-I.Itoh, *The Significance of Medium- or Small-size Devices in Fusion Research*; Oct. 1990
- NIFS-59 A.Fukuyama, S.-I.Itoh, K.Itoh, K.Hamamatsu, V.S.Chan, S.C.Chiu, R.L.Miller and T.Ohkawa, *Nonresonant Current Drive by RF Helicity Injection*; Oct. 1990
- NIFS-60 K.Iida, H.Yamada, H.Iguchi, S.Hidekuma, H.Sanuki, K.Yamazaki and CHS Group, *Electric Field Profile of CHS Heliotron/Torsatron Plasma with Tangential Neutral Beam Injection*; Oct. 1990

- NIFS-61 T.Yabe and H.Hoshino, *Two- and Three-Dimensional Behavior of Rayleigh-Taylor and Kelvin-Helmholz Instabilities*; Oct. 1990
- NIFS-62 H.B. Stewart, *Application of Fixed Point Theory to Chaotic Attractors of Forced Oscillators*; Nov. 1990
- NIFS-63 K.Konn., M.Mituhashi, Yoshi H.Ichikawa, *Soliton on Thin Vortex Filament*; Dec. 1990
- NIFS-64 K.Itoh, S.-I.Itoh and A.Fukuyama, *Impact of Improved Confinement on Fusion Research*; Dec. 1990
- NIFS -65 A.Fukuyama, S.-I.Itoh and K. Itoh, *A Consistency Analysis on the Tokamak Reactor Plasmas*; Dec. 1990
- NIFS-66 K.Itoh, H. Sanuki, S.-I. Itoh and K. Tani, *Effect of Radial Electric Field on α -Particle Loss in Tokamaks*; Dec. 1990
- NIFS-67 K.Sato, and F.Miyawaki, *Effects of a Nonuniform Open Magnetic Field on the Plasma Presheath*; Jan.1991
- NIFS-68 K.Itoh and S.-I.Itoh, *On Relation between Local Transport Coefficient and Global Confinement Scaling Law*; Jan. 1991
- NIFS-69 T.Kato, K.Masai, T.Fujimoto, F.Koike, E.Källne, E.S.Marmar and J.E.Rice, *He-like Spectra Through Charge Exchange Processes in Tokamak Plasmas*; Jan.1991
- NIFS-70 K. Ida, H. Yamada, H. Iguchi, K. Itoh and CHS Group, *Observation of Parallel Viscosity in the CHS Heliotron/Torsatron* ; Jan.1991
- NIFS-71 H. Kaneko, *Spectral Analysis of the Heliotron Field with the Toroidal Harmonic Function in a Study of the Structure of Built-in Divertor* ; Jan. 1991
- NIFS-72 S. -I. Itoh, H. Sanuki and K. Itoh, *Effect of Electric Field Inhomogeneities on Drift Wave Instabilities and Anomalous Transport* ; Jan. 1991
- NIFS-73 Y.Nomura, Yoshi.H.Ichikawa and W.Horton, *Stabilities of Regular Motion in the Relativistic Standard Map*; Feb. 1991
- NIFS-74 T.Yamagishi, *Electrostatic Drift Mode in Toroidal Plasma with Minority Energetic Particles*, Feb. 1991
- NIFS-75 T.Yamagishi, *Effect of Energetic Particle Distribution on Bounce Resonance Excitation of the Ideal Ballooning Mode*, Feb. 1991
- NIFS-76 T.Hayashi, A.Tadei, N.Ohyabu and T.Sato, *Suppression of Magnetic Surface Breeding by Simple Extra Coils in Finite Beta Equilibrium of Helical System*; Feb. 1991

- NIFS-77 N. Ohya, *High Temperature Divertor Plasma Operation*; Feb. 1991
- NIFS-78 K.Kusano, T. Tamano and T. Sato, *Simulation Study of Toroidal Phase-Locking Mechanism in Reversed-Field Pinch Plasma*; Feb. 1991
- NIFS-79 K. Nagasaki, K. Itoh and S. -I. Itoh, *Model of Divertor Biasing and Control of Scrape-off Layer and Divertor Plasmas*; Feb. 1991
- NIFS-80 K. Nagasaki and K. Itoh, *Decay Process of a Magnetic Island by Forced Reconnection*; Mar. 1991
- NIFS-81 K. Takahata, N. Yanagi, T. Mito, J. Yamamoto, O.Motojima and LHDDesign Group, K. Nakamoto, S. Mizukami, K. Kitamura, Y. Wachi, H. Shinohara, K. Yamamoto, M. Shibui, T. Uchida and K. Nakayama, *Design and Fabrication of Forced-Flow Coils as R&D Program for Large Helical Device*; Mar. 1991
- NIFS-82 T. Aoki and T. Yabe, *Multi-dimensional Cubic Interpolation for ICF Hydrodynamics Simulation*; Apr. 1991
- NIFS-83 K. Ida, S.-I. Itoh, K. Itoh, S. Hidekuma, Y. Miura, H. Kawashima, M. Mori, T. Matsuda, N. Suzuki, H. Tamai, T.Yamauchi and JFT-2M Group, *Density Peaking in the JFT-2M Tokamak Plasma with Counter Neutral Beam Injection* ; May 1991
- NIFS-84 A. Iiyoshi, *Development of the Stellarator/Heliotron Research*; May 1991
- NIFS-85 Y. Okabe, M. Sasao, H. Yamaoka, M. Wada and J. Fujita, *Dependence of Au⁺ Production upon the Target Work Function in a Plasma-Sputter-Type Negative Ion Source*; May 1991
- NIFS-86 N. Nakajima and M. Okamoto, *Geometrical Effects of the Magnetic Field on the Neoclassical Flow, Current and Rotation in General Toroidal Systems*; May 1991
- NIFS-87 Sanae -I. Itoh, K. Itoh, A. Fukuyama, Y. Miura and JFT-2M Group, *ELMy-H mode as Limit Cycle and Chaotic socillations in Tokamak Plasmas*, May 1991
- NIFS-88 N.Matsunami and K.Kitoh, *High Resolution Spectroscopy of H⁺ Energy Loss in Thin Carbon Film*; May 1991
- NIFS-89 H. Sugama, N. Nakajima and M.Wakatani, *Nonlinear Behavior of Multiple-Helicity Resistive Interchange Modes near Marginally Stable States*; May 1991
- NIFS-90 H. Hojo and T.Hatori, *Radial Transport Induced by Rotating RF Fields and Breakdown of Intrinsic Ambipolarity in a Magnetic Mirror*; May 1991